LANGMUIR

pubs.acs.org/Langmuir Article

Surface-Functionalized Polystyrene Nanoparticles Alter the Transmembrane Potential via Ion-Selective Pores Maintaining Global Bilayer Integrity

D. Aurora Perini, Elisa Parra-Ortiz, Inmaculada Varó, María Queralt-Martín, Martin Malmsten, and Antonio Alcaraz*

Cite This: *Langmuir* 2022, 38, 14837−14849 Read Online

ACCESS | Metrics & More | Article Recommendations | Supporting Information

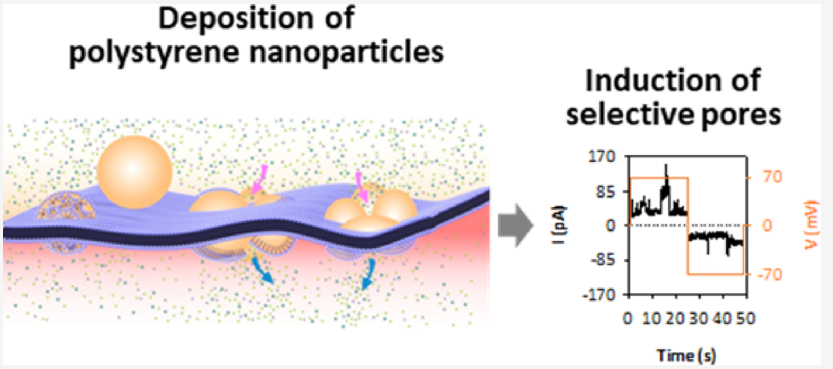

ABSTRACT: Although nanoplastics have well-known toxic effects toward the environment and living organisms, their molecular toxicity mechanisms, including the nature of nanoparticle−cell membrane interactions, are still under investigation. Here, we employ dynamic light scattering, quartz crystal microbalance with dissipation monitoring, and electrophysiology to investigate the interaction between polystyrene nanoparticles (PS NPs) and phospholipid membranes. Our results show that PS NPs adsorb onto lipid bilayers creating soft inhomogeneous films that include disordered defects. PS NPs form an integral part of the generated channels so that the surface functionalization and charge of the NP determine the pore conductive properties. The large difference in size between the NP diameter and the lipid bilayer thickness (∼60 vs ∼5 nm) suggests a particular and complex lipid−NP assembly that is able to maintain overall membrane integrity. In view of this, we suggest that NP-induced toxicity in cells could operate in more subtle ways than membrane disintegration, such as inducing lipid reorganization and transmembrane ionic fluxes that disrupt the membrane potential.

INTRODUCTION

Polystyrene nanoparticles (PS NPs) are produced for a variety of technological applications. Primary uses of such particles include pharmaceuticals, cosmetics, paints, medical and electronic devices, plastic packaging, and construction materials.[1−5] As a result of this, nanometer-sized PS is abundantly present in the environment due to accidental release of produced NPs[6,7] but also due to degradation of bulk PS via mechanical breakdown,[8] UV degradation,[9,10] and/or biodegradation.[11] Given that both micro- and nanoplastics have been detected mostly in a watery environment,[1] ecotoxicological studies have paid special attention to aquatic species, demonstrating that PS NPs could accumulate in tissues, alter the immune system, produce cell damage, and/or induce oxidative stress and genotoxicity, which affect survival, growth, and reproduction.[4,12−17]

Cell membranes are the primary protective barrier of living organisms against toxic agents[8,18] and particularly NPs.[19] NP−membrane interactions involve a complex balance between elastic and adhesion forces that define the degree of membrane deformation and NP wrapping by lipids.[20] Given their hydrophobic nature, noncross-linked plastic NPs could potentially dissolve in the hydrophobic core of bilayers[21] as shown by molecular dynamics simulations for globular polyethylene NPs with a diameter of few nanometers. However, it is unclear whether this mechanism is viable for large NPs (d > 50 nm) exceeding by more than one order of magnitude the bilayer thickness. Possible scenarios for such

Received: September 9, 2022
Revised: November 10, 2022
Published: November 23, 2022

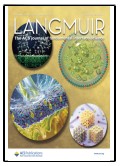

large NPs include full NP engulfment (similar to nonspecific endocytosis), partial wrapping, NP adsorption to the membrane external surface,[20] or disintegration of the NP into individual polymer chains.[22]

Interestingly, cell culture experiments show that cellular binding of NPs disrupts the membrane potential, not only altering the normal cell cycle progression but also inducing malignant transformations and avoiding tissue regeneration.[23] In vitro techniques taking advantage of the fact that PS NPs can be adsorbed on model membranes[24−29] have stimulated intense research providing molecular details not visible at the cellular level. Thus, the alteration of ionic gradients around cells by PS NPs has been linked to a variety of molecular mechanisms such as NP internalization,[30] local collapse of membrane integrity,[25] creation of hydrophilic pores,[31] or even the physical blockage of ion channels such as K^+ or Na^+ ones.[23] These mechanisms are not mutually exclusive but could operate in concert or even synergistically. For instance, in membranes where large NPs are present, pore formation can provide a stabilizing mechanism releasing membrane tension and avoiding global membrane rupture.[19] Thus, the presence of defects or pores in the membrane could impact the membrane potential in two ways: on the one hand, allowing the unassisted transport of hydrophilic solutes and salt ions, and on the other, altering the passive lipid translocation (lipid flip-flop) required for mechanical stability and membrane protein activity.[32]

To gain insight into nanoplastic−membrane interactions, we combined experimental techniques in which 60 nm PS NPs with different surface functionalizations interact with membranes mimicking the phospholipid composition of those from endoplasmic reticulum, mitochondria, lysosome[33−35] or the *Artemia franciscana* brine shrimp eyes,[36−38] a model species particularly relevant in NP aquatic toxicology.[15,39−41] Dynamic light scattering (DLS) was employed to provide colloidal characterization of the NPs in terms of ζ-potential, size, and polydispersity at biologically relevant pH and salinity. Afterward, the surface-sensitive technique quartz crystal microbalance with dissipation monitoring (QCM-D) was used to investigate the NP deposition in real time on supported lipid bilayers and subsequent changes in membrane viscoelasticity. Finally, electrophysiology experiments on planar lipid membranes assessed the membrane integrity upon addition of PS NPs and the potential occurrence of pore formation by monitoring conductivity changes. We observe that under physiological conditions, the studied NPs attach to the lipid surface and form disordered conductive pores that resemble proteolipid pores formed by association of membrane proteins and lipid molecules.[42−52] By using a combination of different electrophysiological parameters, we elucidate the conductive nature of the observed pores, the participation of PS NPs in their structure, and the role of NP charge and functionalization. Based on this, we discuss the possible role of NP-induced pores and their role for membrane organization in nanoplastic toxicology.

Our systematic investigation on model biological membranes using a combination of techniques could be of much interest to elucidate the role of surface chemistry on the propensity of all engineered nanomaterials (both carbon-based and inorganic) to disrupt cell membranes, paving the way to design safer biocompatible particles suitable for environmental and biotechnological applications.[53]

EXPERIMENTAL SECTION

Materials. Three types of NPs (60 nm diameter) were purchased from Magsphere Inc. (Pasadena, CA) and included: nonfunctionalized polystyrene (PS) (plain NP according to manufacturer's nomenclature), aminated polystyrene (PS-NH_2), and carboxylated polystyrene (PS-COOH). Lipids dissolved in chloroform, 1,2-dioleoyl-*sn*-glycero-3-phosphocholine (DOPC), 1,2-dioleoyl-*sn*-glycero-3-phospho-L-serine (DOPS), and 1,2-dioleoyl-*sn*-glycero-3-phosphoethanolamine (DOPE) were purchased from Avanti Polar Lipids (Alabaster, AL). Sodium chloride and 4-(2-hydroxyethyl)-1-piperazineethanesulfonic acid (HEPES) were obtained from Merck KGaA (Darmstadt, Germany). All solutions were prepared using ultrapure water (UW) (Simplicity UV, Merck KGaA, Darmstadt, Germany) with a resistivity of 18.2 MΩ/cm at 25 °C and filtered through a 0.20 μm pore size filter (Scharlau, Spain).

NP Characterization. PS NPs were analyzed at different salt concentrations by DLS using a Zetasizer Nano ZSP (Malvern Panalytical Ltd., Malvern, UK) at a scattering angle of 173° to characterize the hydrodynamic sizes and ζ-potentials. For size determination, three sets of measurements of 10 runs of 10 s were used, whereas ζ-potentials were determined based on 30 runs and monomodal analysis. Automatic attenuation was used for all samples. The ζ-potential values were calculated from the electrophoretic mobility by applying the Smoluchowski equation.[54] Measurements were performed in triplicate at T = 25.0 ± 0.5 °C and reported as the mean ± standard deviation.

Preparation of Liposomes. Small unilamellar vesicles (SUVs) for QCM-D were prepared following a previously described methodology.[55] Briefly, dry lipid films were obtained by mixing DOPC, DOPE, and DOPS stocks in chloroform (10 mg/mL) at a ratio of 5:3:2 (w/w) under an argon atmosphere. Chloroform was then evaporated under an N_2 flow and 2 h vacuum. The dry films were stored under argon at −20 °C. Multilamellar vesicles were prepared at the desired final concentration by hydrating the dry films in UW using eight cycles of 60 s in an ultrasonication bath and 30 s of vortexing at 22 °C. Four 5 min cycles of tip probe sonication (UP50H, Hielscher Ultrasonics GmbH, Germany) (including 2 min in between to cool down the sample and minimize lipid damage by heat[56]) were used to obtain SUVs with final sizes of around 30 nm. The liposome charge and size were characterized by DLS following the same protocol as for NP characterization.

QCM-D. QCM-D measurements were performed using a QSense analyzer (Biolin Scientific, Sweden), and silica-coated sensors (QSense QSX 303 SiO_2, 4.95 ± 0.05 MHz, 14 mm diameter, 0.3 mm thickness, and a mass sensitivity factor of 17.7 ng/cm^2) (Figure S6) were used as substrates for DOPC/DOPE/DOPS (5:3:2) bilayers as described previously.[57] Cleaning and the rest of the experimental procedure were performed as described previously.[55] Briefly, the tubing and the cells were thoroughly cleaned with a 2% Hellmanex solution and multiple UW rinses, combined with bath sonication, followed by rinsing with pure ethanol and drying under an N_2 flow. Before the cell assembly, the silica surfaces were washed in 2% Hellmanex, UW, and finally ethanol, dried with N_2, and plasma-cleaned (Model PDC-32G, Harrick Plasma, USA) for 2 min.

During the experiments, a flow rate of 0.1 mL/min (Ismatec IPC 4-channel peristaltic pump, Cole-Parmer GmbH, Germany) and a constant temperature of 25 °C were set. To form the supported lipid bilayers (SLBs), first UW was pumped until reaching a stable baseline for at least 5 min. To promote bilayer formation in the presence of anionic lipid headgroups, prior to injecting the SUV suspensions, the temperature was increased to 37 °C and a solution of 2 mM $CaCl_2$ was flushed for 5 min. This was a necessary step to obtain stable bilayers made of negatively charged lipids and has previously been demonstrated to result in full surface coverage and largely defect-free bilayers in related systems.[58,59] Efficient bilayer formation, in turn, is important for reducing any direct influence of the negatively charged silica surface on NP interactions, as reported for positively charged peptides.[60] After bilayer formation, excess liposomes and $CaCl_2$ were removed by extensive rinsing with UW, after which the temperature

https://doi.org/10.1021/acs.langmuir.2c02487
Langmuir 2022, 38, 14837−14849

was decreased to 25 °C. SUV deposition, rupture, and full bilayer formation were confirmed by frequency changes (ΔF) of -23 ± 1 Hz and dissipation changes (ΔD) of $(0.25 \pm 0.25) \times 10^{-6}$ with respect to UW (Figure S2). Following bilayer formation, 150 mM NaCl buffered with 5 mM HEPES at pH 7.4 was pumped for 10 min, and the NP sample was pumped for 1 h onto the SLBs at 100 ppm in the same saline buffer. For quantification, the seventh harmonic was chosen for maximum data robustness.[24,55] When the adsorbed PS NPs formed a homogeneous film and the dissipative energy losses were small ($\Delta D/\Delta F < 1 \times 10^{-7}$ Hz^{-1} for all overtones,[61] normalized ΔF equal for each overtone[62]), the Sauerbrey equation was used to calculate the deposited mass Δm from the frequency variations:[63−65]

$$\Delta m = -\frac{\Delta F_n}{n} c$$

where ΔF_n is the measured frequency shift at overtone number n and C is the mass sensitivity constant that equals 17.7 ng/Hz cm^2. Measurements were conducted in triplicate and reported as the mean ± standard deviation.

Planar Bilayer Formation and Electrical Measurements. Planar membranes were obtained by apposition of two lipid monolayers in a Teflon chamber separated in two compartments of 1.6 mL each (so-called cis and trans) by a 15 μm-thick Teflon film with a central orifice of 70−100 μm diameter, using a solvent-free modified Montal−Mueller technique[66,67] (Figure S7). In brief, the lipid was prepared by dissolving DOPC/DOPE/DOPS (5:3:2 w/w) in pentane at 5 mg/mL after chloroform evaporation under argon. The orifice was pretreated with a 1% solution of hexadecane in pentane. After pentane evaporation, both the cis and trans compartments were filled with the desired saline buffer using syringes, and 10−20 μL aliquots of the lipid solution were deposited on the surfaces of both subphases to form two monolayers. The solvent was allowed to evaporate for 10 min. Then, the level of the solution in each compartment was raised above the hole, so the planar bilayer was formed by monolayer apposition at both sides of the hole. PS NP stock solutions prepared at 10,000 ppm were sonicated and vortexed to ensure full dispersion before their addition to the cis side of the chamber, and they were added at a final concentration of 100 ppm.

To record NP-induced electrical currents through the planar membrane, once the particles were added, a periodic voltage sweep was applied, composed of 70 mV for 24 s followed by −70 mV for another 24 s, as described in ref 25. This voltage difference was applied using home-built Ag/AgCl electrodes in 2 M KCl with 1.5% agarose bridges assembled within standard 250 μL pipette tips. The potential was defined as positive when it was higher at the side of NP addition (cis side), whereas the trans side was set to ground. An Axopatch 200B amplifier (Molecular Devices, Sunnyvale, CA) in the voltage clamp mode was used to measure the current and the applied potential. Current was filtered with a 5 kHz 8-pole in-line Bessel filter and digitized with a Digidata 1440A (Molecular Devices, Sunnyvale, CA) at a 20 kHz sampling frequency. The membrane chamber and the headstage were isolated from external noise sources with a double metal screen (Amuneal Manufacturing Corp., Philadelphia, PA). Conductance values were obtained from current measurements in symmetrical salt solutions of 150 mM NaCl buffered with 5 mM HEPES at pH 7.4 with NPs added at a final concentration of 100 ppm. The conductance values were evaluated using the Gaussian fit tool of Clampfit 10.7 (Molecular Devices, Sunnyvale, CA). The cation versus anion preference of NP-induced currents was assessed by measuring the reversal potential (RP), that is, the applied voltage needed to precisely cancel the current measured when a given salt concentration gradient is applied to the system. For these RP experiments, planar membranes of either DOPC/DOPE/DOPS (5:3:2 w/w) or DOPC/DOPE (7:3 w/w) were formed under fivefold (50 mM/250 mM NaCl) concentration gradients, and the net ionic current obtained was manually set to zero by adjusting the applied potential. This potential was then corrected by subtracting or adding (depending on the salt gradient orientation) the liquid junction potential of the electrode salt bridges[68] to obtain the RP. The measured RP was converted into a channel permeability ratio P_+/P_- by means of the Goldman−Hodgkin−Katz equation.[69] In these assays, the final NP concentration at the cis side was increased to 200 ppm for PN-NH$_2$ and to 500 ppm in the case of PS and PS-COOH to ensure enough pore formation events.

RESULTS AND DISCUSSION

NP Aggregation, Size, and ζ-Potential. We first used the DLS to characterize the colloidal properties of NPs under different conditions, as shown in Figure 1. Results in UW

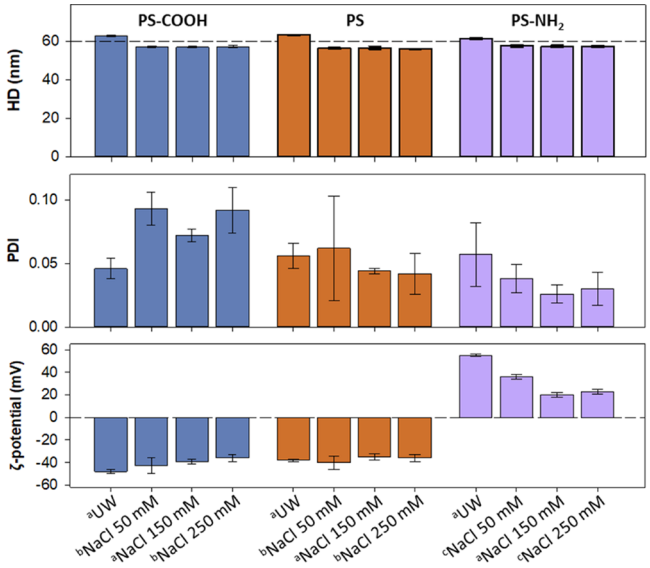

Figure 1. DLS characterization of PS NPs at different concentrations in UW and in NaCl buffered with 5 mM HEPES at pH 7.4, showing the hydrodynamic diameter (HD, upper panel), polydispersity index (PDI, middle panel), and ζ-potential (lower panel). [a]100 ppm; [b]500 ppm; and [c]200 ppm.

confirm the manufacturer data, and the three NP suspensions shown are essentially monodispersed (PDI < 0.2) with an average diameter of approximately 60 nm. In NaCl solutions at pH 7.4, the NPs showed a slight reduction (∼10%) of their size while monodispersity was maintained. Importantly, no aggregation was found for any NP under the conditions investigated during the time period (1−2 h) comparable to that of QCM-D and electrophysiological experiments reported later in the study. To highlight the importance of this initial characterization, note that NPs with amidine functionalization were discarded from our study because DLS measurements showed aggregation in NaCl solutions (Figure S1).

As regard to ζ-potential, PS-COOH showed negative values whereas PS-NH$_2$ displayed positive ones, as expected from the presence of either negatively charged carboxyl groups (PS-COOH) or positive amines (PS-NH$_2$). However, plain (according to manufacturer's nomenclature) PS NPs yielded negative zeta potential values similar to those found for PS-COOH, which is attributable to the sulfate groups resulting from the persulfate initiator used in the PS emulsion polymerization process as reported by the manufacturer (Magsphere Inc.).[70]

NP Interactions with Supported Lipid Membranes. To assess the interaction between PS NPs and model lipid membranes, we employed QCM-D, a technique that allows real-time monitoring of the formation and stability of thin films.[24,28,57,61,63,65,71−73] We formed DOPC/DOPE/DOPS (5:3:2 w/w) SLBs based on the phospholipid headgroups

https://doi.org/10.1021/acs.langmuir.2c02487
Langmuir 2022, 38, 14837−14849

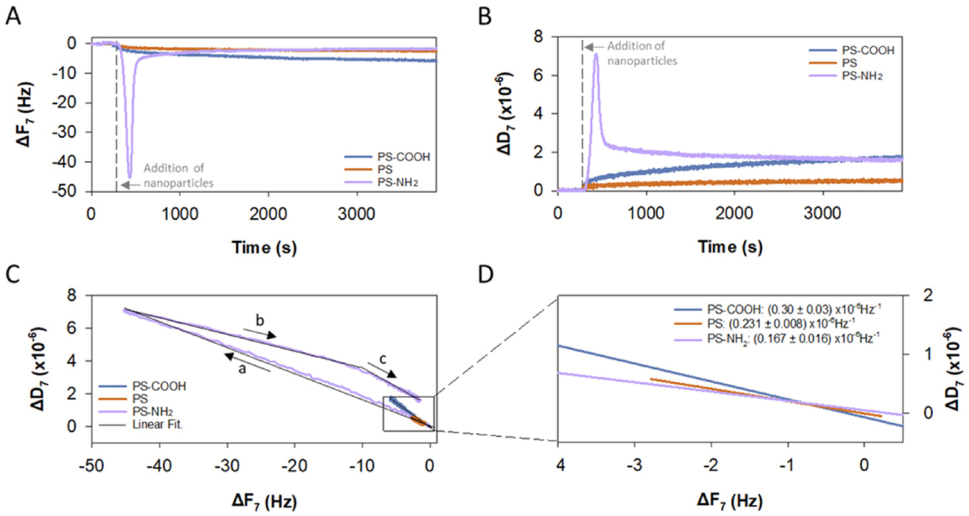

Figure 2. Representative QCM-D measurements of changes in frequency (ΔF) (A) and dissipation (ΔD) (B) at the seventh overtone during deposition of a NP suspension (in 150 mM NaCl with 5 mM HEPES at pH 7.4) on 5:3:2 DOPC/DOPE/DOPS bilayers. A plot of ΔD vs ΔF (C) and comparison of the obtained slopes in panel (C) (absolute values; slope *a* was considered for PS-NH_2) (D). In panels (A and B), the reference line indicates the start of NP suspension addition (t = 300 s). In panel (C), the arrows indicate the evolution of slopes with time.

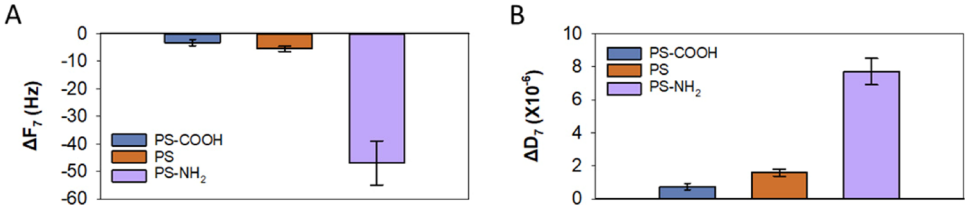

Figure 3. QCM-D maximum change in frequency and dissipation measured for the seventh overtone after PS NP deposition in 150 mM NaCl with 5 mM HEPES at pH 7.4 on a supported 5:3:2 DOPC/DOPE/DOPS bilayer. The maximum change of PS-COOH and PS corresponds to the final equilibrium value (n = 3).

mainly composing cell membranes such as those of the endoplasmic reticulum, mitochondria, and lysosome.[33−35] Of note, this composition is similar to the membrane of the *Artemia franciscana* brine shrimp eyes,[36−38] a species widely used in toxicology and particularly to assess the toxicity of plastic NPs.[15,39,74−76]

After SLB formation at 37 °C, full surface coverage and absence of noncollapsed SUVs were confirmed (Figure S2) in line with previous results[57,77,78] and studies where neutron reflectometry was used to demonstrate defect-free bilayers.[55,79] The addition of different PS NPs to such preformed lipid bilayers (performed at 25 °C) induced an increase in mass of the resonator detectable by a decrease in frequency (ΔF) and an increase in dissipation (ΔD) (Figures 2A,B and 3). This indicates that all studied PS NPs are able to reach the bilayer surface and interact with the SLB, with the positively charged PS-NH_2 showing the largest changes (by an order of magnitude) both in frequency and dissipation (Figure 3).

Time evolution of ΔF and ΔD shows additional qualitative trends not visible in Figure 3. PS and PS-COOH (Figure 2A,B) show small changes (a decrease in frequency and an increase in dissipation) that increase gradually with time until reaching a quasi-equilibrium (Figure S3). In contrast, PS-NH_2 shows nonmonotonical dramatic changes in both frequency and dissipation. Thus, a quick initial peak is followed by a slow decay, leading to saturation values of $\Delta F = -1.2 \pm 0.7$ Hz and $\Delta D = (1.3 \pm 0.3) \times 10^{-6}$, comparable to those of the other two NPs (Figures 2A,B and 3).

Such contrasting features are visible in ΔD versus ΔF plots (Figure 2C) that may reflect the viscoelastic properties of the adsorbed layers and also hydrodynamic effects.[80] PS and PS-COOH NPs display one single $\Delta D/\Delta F$ slope, whereas PS-NH_2 NP presents a more complex pattern with different regions (see Figure 2C). Large values of $\Delta D/\Delta F$ ratios are commonly associated with soft, flexible, and hydrated film conformations, whereas low values are usually observed in dehydrated rigid structures.[62,71,81−83]Figure 2D shows a zoomed-in section of Figure 2C for the lowest values of ΔD and ΔF. Considering that the $\Delta D/\Delta F$ slope in Figure 2D is lower for PS-NH_2, followed by PS and PS-COOH, and the fact that the film stiffness increases with the strength of NP adsorption, we conclude that PS-NH_2 has the highest affinity for the bilayer followed by PS and PS-COOH.

The complex behavior of PS-NH_2 deserves further explanation. A close inspection of Figure 2C (arrows showing the time evolution) indicates the occurrence of at least two regimes. The first of these (Figure 2C arrow a) suggests the continuous incorporation of positive NPs to the lipid film causing destabilization of the initially confluent lipid bilayer by interfacial reactions such as osmotic dehydration.[81,84] The second regime is characterized by gradients of $\Delta D/\Delta F$ having an opposite sign to the first stage with two different slopes (Figure 2C arrow b and arrow c) suggesting a transition to a more dissipative structure than in the other NPs that results from the instability of the rigid bilayer created after the initial stage (see Figure S4 for additional details). Because PS-NH_2 displays a much higher dissipation than that seen for PS and

https://doi.org/10.1021/acs.langmuir.2c02487
Langmuir 2022, 38, 14837−14849

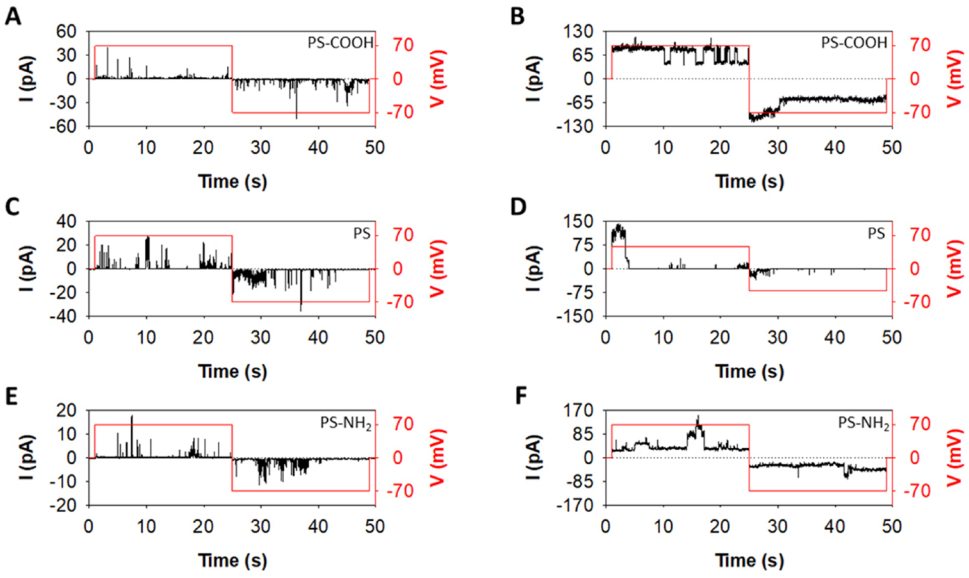

Figure 4. Representative currents induced by PS-COOH (A,B), PS (C,D), and PS-NH2 (E,F). Panels (A,C,E) show how addition of NPs induces transient current spikes so short-lasting that quantification of the average current is not possible. Panels (B,D,F) display example traces in which NP addition yields stepwise current jumps of variable but well-defined conductance levels.

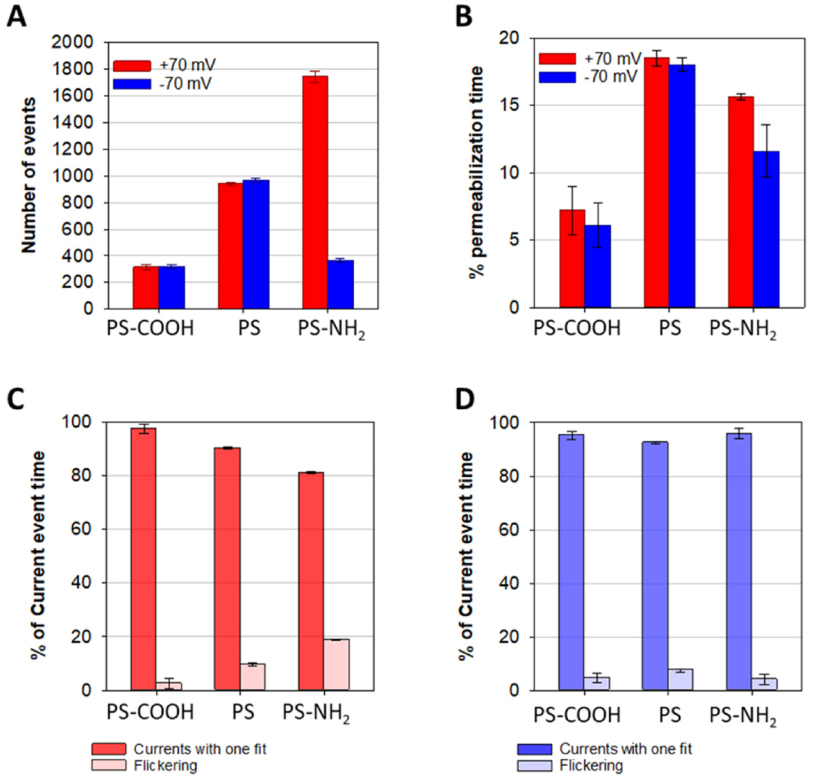

Figure 5. Number of events (A) and percentage of recorded time with nonzero current levels (% permeabilization time, B). Percentage of current time with defined conducting levels and flickering events at positive (C) and negative (D) applied voltages. Errors were calculated using error propagation.

PS-COOH, we believe that the observed changes are not purely hydrodynamic effects but instead attributable to a different interaction with the lipid bilayer. Thus, we hypothesize that PS-NH_2 particularly enhances lipid extraction from the supported film[27] and/or the creation of water defects that induce lipid reorganizations[32,85] (Figure S5). Such extraction of anionic phospholipids and lipid removal have been observed also for other cationic NPs.[27,86,87] Overall, the finding that the final ΔD after NP exposure was higher than the initial value indicates that soft films of an inhomogeneous structure are obtained for the three PS NPs under study (Figure 2C,D). Further analysis of the interaction by complementary techniques such as scattering-based microscopy methods,[88] which may provide additional information on NP adsorption into the SLBs, are out of the scope of the present study.

https://doi.org/10.1021/acs.langmuir.2c02487
Langmuir 2022, 38, 14837−14849

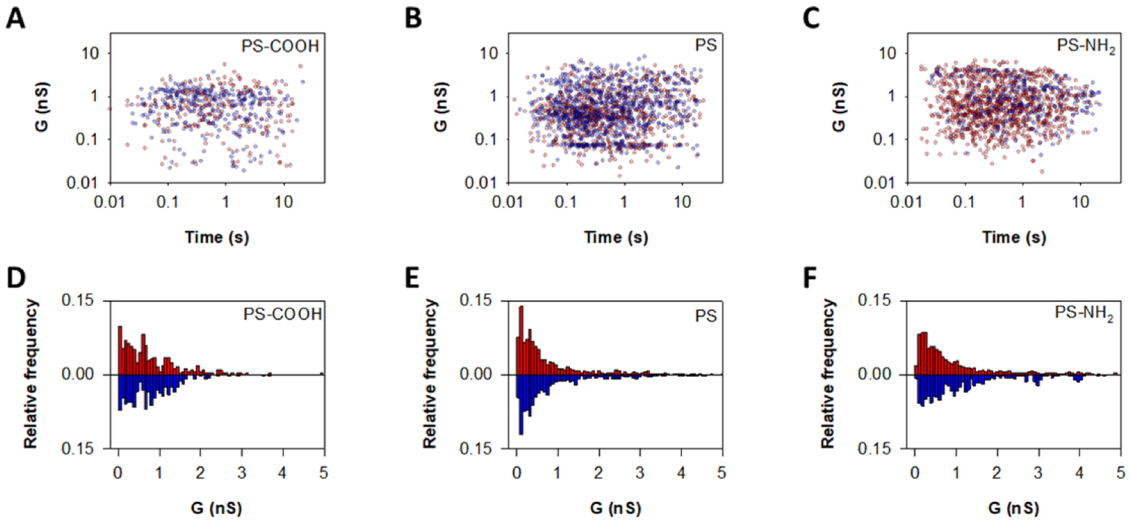

Figure 6. Correlation between event conductance and time length for PS-COOH (A), PS (B), and PS-NH_2 (C). NP-induced conductance levels at positive (red) and negative (blue) applied voltages for PS-COOH (D), PS (E), and PS-NH_2 (F).

NP-Induced Currents in Planar Model Membranes. To evaluate potential membrane permeabilization, we next prepared planar bilayers by apposition of two monolayers made of DOPC/DOPE/DOPS in a 5:3:2 ratio (w/w) in 5 mM HEPES at pH 7.4 with 150 mM NaCl following the Montal–Mueller technique.[67] This approach provides very stable solvent-free membranes in which spontaneous permeabilization in the absence of NPs was found to be nonexistent. After NP addition to the cis chamber of the cell, voltage differences of ±70 mV were applied between both sides of the cell in periodic intervals and the transmembrane current was measured. By using this protocol, we investigate the influence of voltage polarity and NP charge on the NP–membrane interaction.[25] Also, we simulate, as a first approximation, the conditions of living cells where the concerted interplay of ion channels generates dynamic changes in both membrane potential (∼ ±100 mV)[89,90] and ionic fluxes.[91,92]

Figure 4 shows the representative traces of the ion currents induced by PS-COOH (A,B), PS (C,D), and PS-NH_2 (E,F) displaying a variety of current levels that fluctuate with time. For each PS NP, either transient current spikes (Figure 4A,C,E) or well-defined stepwise current jumps (Figure 4B,D,F) were found for both voltage polarities, similar to those caused by proteins forming membrane defects such as aqueous pores.[21] Importantly, all NPs considered in our study are able to induce membrane permeability without leading to global membrane disintegration. The finding of the conservation of membrane integrity, a capital issue to distinguish between NP binding and internalization in cells,[23] is in line with the previous findings for the interaction between PS particles of different sizes (from 20 nm to ∼2 μm) and giant unilamellar vesicles.[93−95]

In a previous study following a similar voltage protocol as the one used here,[25] PS-NH_2 induced progressively increasing currents that finally lead to membrane disintegration, whereas PS-COOH failed to induce membrane permeability.[25] Such differences with our present findings could originate either from differences in bilayer preparation (liposome addition to parallel array platforms there) or from differences in membrane compositions (the previous study including also cholesterol and cerebroside[25]).

Assessment of Membrane Permeabilization by NPs. Given the similarity between the NP-induced current traces and those caused by membrane proteins, we use quantification methods employed in the analysis of ion channel activity, such as the number of events. An event is the time period of a current trace with a well-defined conducting level (i.e., the histogram of current values can be represented by a single peak) (see Experimental Section). The number of current events induced by each type of NP is shown in Figure 5A to clearly illustrate the results. Thus, PS-COOH NPs show little membrane disruption, without any observable influence of voltage polarity. PS-NH_2 under $V < 0$, in turn, shows a number of events compared to PS-COOH. In contrast, for positive voltages, in which the positively charged NPs are forced to go toward the bilayer, the number of events displays a fivefold increase compared to that observed for the opposite polarity. Nonfunctionalized PS, finally, represents an intermediate case, showing no dependence on the sign of the applied voltage.

The time variability of current traces in Figure 4 suggests that the number of events shown in Figure 5A could be insufficient to assess the membrane permeability. That is, one type of NP displaying many events of short duration may have a similar permeabilization capacity to another type of NP with few, but longer, events. To address this issue, the fraction of the total experimental time in which NP-induced currents were present is shown in Figure 5B. PS-COOH NPs show the lowest values (∼6%) whereas nonfunctionalized PS NPs show the largest ones (almost 20%), being largely insensitive to the voltage polarity, in line with the data in Figure 5A.

The case of PS-NH_2 is particularly complex as the large number of events at the positive voltage in Figure 5A does not lead to longer permeabilization times in Figure 5B. Indeed, PS-NH_2 NPs in Figure 5B show lower time fractions than PS, and the dependence on voltage polarity is clearly reduced in comparison with Figure 5A. To clarify this point, we next classified the events making a distinction between those with well-defined duration and the so-called flickering[96] for positive and negative applied voltages (Figure 5C,D). In practice, flickering corresponds to fast transitions that are unresolved because their life-times are comparable to the sampling time of our protocol (0.05 ms)[97] (see Experimental Section). Interestingly, PS-NH_2 NPs at $V > 0$ show a larger occurrence

https://doi.org/10.1021/acs.langmuir.2c02487
Langmuir 2022, 38, 14837−14849

of flickering, explaining why a large number of events (1744 ± 44, Figure 5A) does not translate to a large time with current events (15.6 ± 0.23%, Figure 5B).

Figure 6A−C shows that there is no correlation between the measured conductance level (G) and the corresponding lifetime, regardless of the NP type and voltage polarity. The randomness of G versus t distributions emphasizes that the observed transmembrane currents correspond to stochastic transitions (successive openings and closings) and not to progressive membrane disintegration. Histograms of conductance values in Figure 6D−F for NP PS-COOH, PS, and PS-NH_2 show considerable dispersion, with the most probable conductance peak at around $G \sim 20-50$ pS and secondary peaks at higher conductance values that extend to several nS. As the first approximation, the pore conductance can be written as $G \sim \kappa\pi r^2/L$ where κ is the electrolyte conductivity ($\kappa \sim 1.7$ S/m for 150 mM NaCl and KCl at pH 7.4) and $L \sim 5$ nm is the pore length assuming that it spans across the distance of the lipid bilayer.[98] This allows a rough estimation of the characteristic pore radius (r), corresponding to $r \sim 0.3$ nm for $G \sim 50$ pS. The upper limit of our conductance measurements ($G \sim 1$ nS) would correspond to $r \geq 1$ nm. Such scattered values in pore dimensions are characteristic of systems forming disordered channel structures where there is not a unique pore configuration but rather a variety of arrangements, as seen for viral proteins[43−51] cell-penetrating peptides,[99] and other small charged peptides.[42,52,100] Note that the myriad of pore configurations, as opposed to that of well-defined canonical ion channels,[96] is seen in a dual way: as a static disorder (existence of different conductive levels in the traces) but also as a dynamic disorder (variation of current levels with time, shown in Figure 6A−C).[101]

A combined measurement of the membrane-disrupting activity of PS NPs could come from the transferred charge Q calculated as the integral of the current over time as shown in Figure 7. As seen from the image, the transferred charge for PS

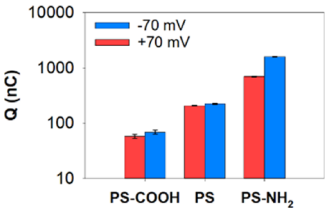

Figure 7. Transferred charge at positive and negative applied voltages. Y-axis is shown in a logarithmic scale. Errors were calculated using error propagation.

is almost four times higher than that for PS-COOH, as could be expected because PS shows a higher number of events and longer times of current events than PS-COOH. Also, both PS and PS-COOH display only minor differences with the voltage polarity in transferred Q. PS-NH_2 is again different because of the larger number of events for $V > 0$ with respect to $V < 0$ (1774 vs 366), which, however, does not imply a higher transference of charge. In fact, it is just the other way around (696 vs 1587 nC). This was motivated by the larger occurrence of flickering at $V > 0$ (Figure 5C,D).

The combined findings of Figures 5−7 reveal that PS-COOH NPs are the least membrane-disruptive of the three NPs investigated, yielding the lowest values in number of events, permeabilization times, and transferred charge. Also, we observe that PS has much higher affinity for DOPC/DOPE/DOPS (5:3:2) membranes than PS-COOH. Considering that both displayed very similar ζ-potentials in Figure 1 and hence similar negative charges, the differences between PS and PS-COOH may have their origin in NP hydrophobicity.[18,24,102,103] In line with this, in our hydrophobicity assay (see Supplementary Information), the surface hydrophobicity was found to be higher for PS than for PS-COOH (Table S1).

Another important finding is that PS-NH_2 NPs display the highest disruption capacity if all factors (Figures 5−7) are taken together. Thus, PS-NH_2 NPs have a similar permeabilization time to PS, but the transferred charge Q is much higher, especially in the voltage polarity where PS-NH_2 NPs are not driven toward the membrane but in the opposite direction. Our results suggest that other factors than purely electrostatic interactions between positive PS-NH_2 and negatively charged lipids[25] play a major role. As shown in Table S1, the surface hydrophobicity of PS-NH_2 is comparable to that of PS and much larger than that for PS-COOH. Interestingly, Mielke and Zimchl[102] reported that the particle−solvent behavior at the interface of hydrophobic materials such as PS NPs is regulated by the hydrophobic/hydrophilic balance that can be maintained (PS-NH_2) or altered (PS-COOH) in the functionalization process.[104] Finally, note that there is a qualitative agreement between QCM-D and electrophysiology about the higher membrane-disruptive capacity of PS-NH_2. However, both techniques are not directly quantitatively comparable because QCM-D encompasses horizontal SLBs formed on glass with NP suspensions being pumped constantly, whereas electrophysiology involves free-standing vertical lipid bilayers and the addition of discrete aliquots of NPs.

Ion Selectivity of NP-Induced Pores. One intriguing issue arising from previous sections is the structure of the permeation pathways created by ∼60 nm NPs on ∼5 nm-thick lipid bilayers. At this point, it is unclear whether NPs are structurally involved in the formation of membrane defects or pores[32] or if their action resembles to the "detergent-like mechanisms" invoked for proteins that just disrupt the lipid packing creating hydrophilic pores.[105,106]

To elucidate how NPs and membrane lipids contribute to the pore structure, we next performed selectivity experiments using a fivefold concentration gradient of NaCl (50 and 250 mM) buffered with 5 mM HEPES at pH 7.4. As shown in Figure 1, there was no NP aggregation under these conditions. We performed experiments using two different membrane compositions, the physiologically relevant DOPC/DOPE/DOPS at a ratio of 5:3:2 (w/w) with 20% negative charge and a neutral membrane DOPC/DOPE at a ratio of 7:3 (w/w).

Figure 8A shows the measured selectivity (shown as the permeability ratio, P_+/P_-) when a charged membrane (DOPC/DOPE/DOPS at a ratio of 5:3:2 (w/w)) is placed under a NaCl concentration gradient of 50/250 mM and PS-COOH, PS, or PS-NH_2 NPs are added to the diluted side. Under these conditions, both PS-COOH and PS NPs create pores with preference for cations, which is consistent with their negative ζ-potential (Figure 1) but also with the negative charge of the membrane. However, experiments with PS-NH_2 NPs show a preference for anions, incompatible with the membrane charge but fully compatible with the positive net charge of the aminated NP revealed by the corresponding ζ-potential (Figure 1).

https://doi.org/10.1021/acs.langmuir.2c02487
Langmuir 2022, 38, 14837−14849

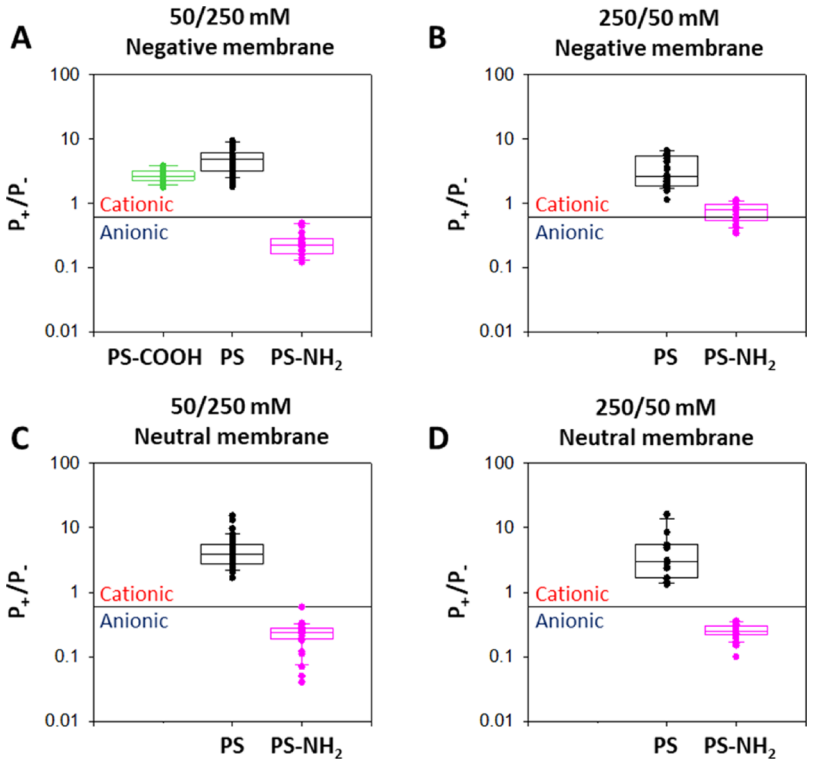

Figure 8. Ion selectivity of NP-induced pores under two salt gradients and two membrane lipid compositions. (A) 50/250 mM NaCl in DOPC/DOPE/DOPS (5:3:2). (B) 250/50 mM NaCl in DOPC/DOPE/DOPS (5:3:2). (C) 50/250 mM NaCl in DOPC/DOPE (7:3). (D) 250/50 mM NaCl in DOPC/DOPE (7:3). All salt solutions were buffered with 5 mM HEPES at pH 7.4. In all panels, the solid lines indicate the limit between cationic and anionic selectivities, located at a P_+/P_- of 0.6 due to the different diffusivities of Na^+ and Cl^- ions. Data are shown as box plots, where the boundary of the box closest to zero indicates the 25th percentile, a line within the box marks the median, and the boundary of the box farthest from zero indicates the 75th percentile. Solid circles correspond to individual experiments. Error bars indicate SD ($n \geq 20$).

Figure 8B displays the selectivity obtained with experiments performed as in Figure 8A but with the opposite salt concentration gradient (250/50 mM) for NPs added to the concentrated side. Under these conditions, we did not obtain permeabilization events with PS-COOH despite increasing the NP concentrations five times up to 500 ppm. In contrast, PS NPs yielded pores with a cationic selectivity similar to that in the 50/250 mM salt gradient (Figure 8A). Importantly, experiments with PS-NH_2 NPs display scattered values that range from anionic selectivity to cationic one (Figure 8B). Positively charged PS-NH_2 NPs alone cannot account for a cation-selective pore, indicating that the negatively charged lipids present in the membrane must participate in the pore structure similar to membrane proteins that assemble with lipids to form joint proteolipidic structures.[42−52]

To inspect the role of lipid charge in the pore selectivity, we also performed experiments in neutral membranes (DOPC/DOPE 7:3 (w/w), Figure 8C,D). PS NPs induced cation-selective pores that were slightly less selective than those in the experiments with a charged membrane, suggesting that both the NP charge and the membrane charge contribute to the overall selectivity. In addition, PS-NH_2 generated anion-selective currents under the two orientations of the concentration gradient explored (50/250 mM (Figure 8C) and 250/50 mM (Figure 8D)). The fact that we did not find any cation-selective pore induced by PS-NH_2 for neutral membranes as in Figure 8B validates the hypothesis that the lipid charge may be responsible for the cation-selective events obtained in that case.

Overall, our results confirm that PS NPs participate in the pore structure to form some kind of a combined arrangement together with lipid molecules that still is able to maintain global membrane integrity under a concentration gradient. In the conditions of our study (100 ppm of NPs and 20% of charged lipids in the 5:3:2 membrane), the selectivity of the induced pores is mainly ruled by the NP charge, including a small but measurable contribution from the membrane charge revealed by the comparison with control experiments in neutral membranes.

CONCLUSIONS

We investigate how different PS NPs induce permeabilization of membranes made of physiologically relevant phospholipid compositions by combining complementary experimental techniques. The combined results of DLS, QCM-D, and electrophysiology experiments indicate that surface functionalization determines the NP−membrane interaction by a combination of different factors. The highest affinity for the negative bilayer found for PS-NH_2 in QCM-D accompanied by the greatest disruption capacity in terms of electrophysiological parameters (number of events, permeabilization time, and transferred charge) suggest an electrostatic NP−membrane mechanism favoring positively charged NPs over negative ones (PS and PS-COOH). However, some findings put into question a purely Coulombic scenario. For instance, the asymmetry found regarding voltage polarity (the highest charge transference in PS-NH_2 appears when NPs are driven outward from the membrane) suggests that lipid restructuring together with NP adhesion to the membrane surface could give

https://doi.org/10.1021/acs.langmuir.2c02487
Langmuir 2022, 38, 14837−14849

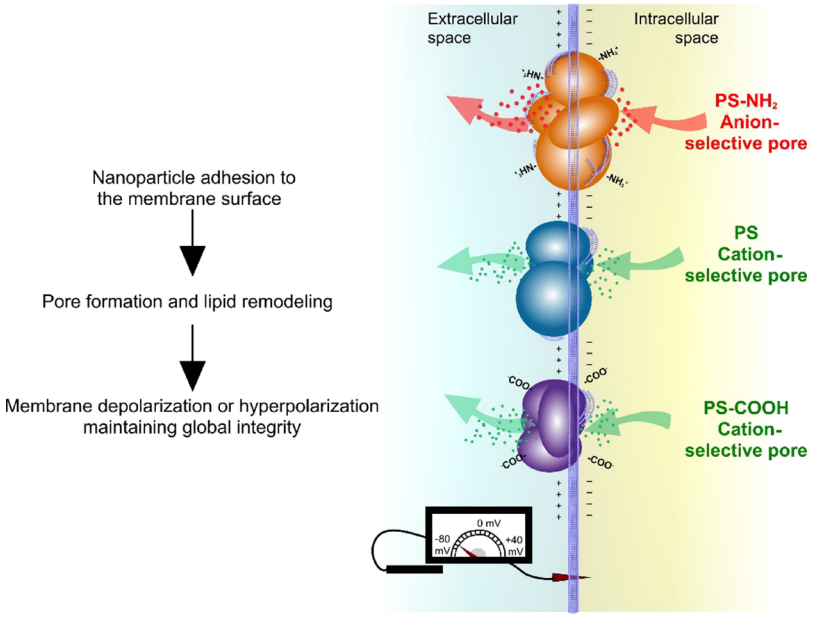

Figure 9. Cartoon illustrating the complex modulation of the cell transmembrane electric potential exerted by PS NPs.

rise to highly inhomogeneous charge distributions with non-Ohmic transport features. Thus, adsorption of positive PS-NH_2 NPs onto a negatively charged membrane could yield bipolar-type charge distributions resembling p−n semiconductor junctions with nonlinear conduction.[107,108] On the other hand, the pronounced differences between PS and PS-COOH with almost identical negative charges also reveal the importance of NP hydrophobicity, as confirmed by absorption measurements of Rose Bengal and in line with the previous studies.[24,102,104,109,110]

The fact that PS NP-induced pores maintain membrane integrity, as opposed to the progressive membrane disintegration found with other bilayer preparations and membrane compositions, has stimulating implications for NP−membrane interactions and nanoplastic toxicology. Concerning membrane architecture and dynamics, it is striking to note the difference in size between NPs (∼60 nm in our case) and typical membrane proteins inducing pores that approximately match the bilayer length (∼5 nm). Although the actual mechanism is still unknown, the NP adhesion leading to partial or total NP wrapping by lipids could involve, in the case of PS NPs, the formation of dissolved styrene clusters.[111] However, it is unclear if these findings obtained for small PS NPs (600 styrene monomers) can be extrapolated to much larger particles of ∼60 nm.

As regard to NP-induced toxicity, the selective hydrophilic pores created by PS NPs point to a more complex modulation of transmembrane electric potential as summarized in the cartoon of Figure 9. Cell membranes are characterized by a net negative charge on the cytosolic side of the membrane (usually −40 to −70 mV[23]) that changes during cell proliferation and differentiation.[23,112] Precedent toxicological studies have demonstrated that NPs could break the cell cycle by inducing not only the most common membrane depolarization[23,113] but also hyperpolarization.[114,115] The fact that cationic NPs are usually more toxic to cells than anionic ones[1,15,116,117] could be tentatively explained in terms of our findings. We have shown that PS-NH_2 has the most potent capacity of membrane disruption, pointing all our findings to membrane depolarization by different mechanisms. First, hypothetical internalization of positively charged PS-NH_2 would decrease the negative membrane potential. Second, selective pores induced by PS-NH_2 are cation-selective for the inward flow but anion-selective for the outward one, suggesting a highly asymmetric membrane charge distribution produced either from NP adhesion or from major lipid reorganizations. Note that both the entrance of positive charges and the exit of negative ones decrease the membrane potential. Interestingly, negatively charged PS and PS-COOH follow the opposite pattern: either by NP internalization or by the charge transferred by their induced selective pores, the membrane potential increases leading to hyperpolarization.

Overall, we hypothesize that PS NPs could act as artificial transmembrane ion transporters altering the cell homeostasis and ultimately inducing cell apoptosis[118,119] by a combination of mechanisms that do not require membrane disintegration but more subtle mechanisms including the passive transport of charges and major membrane reorganizations by direct NP adhesion or NP-induced flip-flop.

■ ASSOCIATED CONTENT

Supporting Information

The Supporting Information is available free of charge at https://pubs.acs.org/doi/10.1021/acs.langmuir.2c02487.

DLS characterization of NPs, supported bilayer formation, NP deposition, hydrophobicity assays, QCM-D scheme, and planar bilayer formation (PDF)

■ AUTHOR INFORMATION

Corresponding Author

Antonio Alcaraz − *Laboratory of Molecular Biophysics, Department of Physics, Universitat Jaume I, 12071 Castellón, Spain;* orcid.org/0000-0002-7830-3189; Phone: +34 964 72 8044; Email: alcaraza@uji.es

https://doi.org/10.1021/acs.langmuir.2c02487
Langmuir 2022, 38, 14837−14849

Authors

D. Aurora Perini − *Laboratory of Molecular Biophysics, Department of Physics, Universitat Jaume I, 12071 Castellón, Spain;* orcid.org/0000-0002-7346-4266

Elisa Parra-Ortiz − *Department of Pharmacy, University of Copenhagen, DK-2100 Copenhagen, Denmark;* orcid.org/0000-0003-2219-8866

Inmaculada Varó − *Institute of Aquaculture Torre de la Sal (IATS-CSIC), 12595 Castellón, Spain;* orcid.org/0000-0002-3937-3846

María Queralt-Martín − *Laboratory of Molecular Biophysics, Department of Physics, Universitat Jaume I, 12071 Castellón, Spain;* orcid.org/0000-0002-0644-6746

Martin Malmsten − *Department of Pharmacy, University of Copenhagen, DK-2100 Copenhagen, Denmark; Department of Physical Chemistry 1, University of Lund, SE-22100 Lund, Sweden*

Complete contact information is available at: https://pubs.acs.org/10.1021/acs.langmuir.2c02487

Author Contributions

The manuscript was written through contributions of all authors. All authors have given approval to the final version of the manuscript.

Funding

This study was funded by the Spanish Government MCIN/AEI/10.13039/501100011033 (project 2019-108434GB-I00 to A.A. and project IJC2018-035283-I to M.Q.-M.), Universitat Jaume I (project UJI-B2018-53 to A.A. and UJI-A2020-21 to M.Q.-M and D.A.P.), Generalitat Valenciana (project GRISOLIAP/2018/061 to D.A.P. and A.A., project AICO/2020/066 to A.A., and grant BEFPI/2020/040 to D.A.P.), the Swedish Research Council (grant numbers 2016-05157 and 2021-05498 to M.M.), the Independent Research Fund Denmark (grant number 9040-00020B to M.M. and E.P.-O.), and the LEO Foundation Center for Cutaneous Drug Delivery (grant number 2016-11-01 to M.M.).

Notes

The authors declare no competing financial interest.

■ ABBREVIATIONS

PS NPs, polystyrene nanoparticles; DLS, dynamic light scattering; QCM-D, quartz crystal microbalance with dissipation monitoring; PS, plain polystyrene; PS-NH_2, aminated polystyrene; PS-COOH, carboxylated polystyrene; DOPC, 1,2-dioleoyl-*sn*-glycero-3-phosphocholine; DOPS, 1,2-dioleoyl-*sn*-glycero-3-phospho-L-serine; DOPE, 1,2-dioleoyl-*sn*-glycero-3-phosphoethanolamine; HEPES, 4-(2-hydroxyethyl)-1-piperazineethanesulfonic acid; UW, ultrapure water; SUVs, small unilamellar vesicles; ΔF, frequency changes; ΔD, dissipation changes; SLB, supported lipid bilayers; PDI, polydispersity index; RP, reversal potential; P_+/P_-, channel permeability; GHK, Goldman−Hodgkin−Katz eq; Q, transferred charge; G, conductance

■ REFERENCES

(1) Kik, K.; Bukowska, B.; Sicińska, P. Polystyrene Nanoparticles: Sources, Occurrence in the Environment, Distribution in Tissues, Accumulation and Toxicity to Various Organisms. *Environ. Pollut.* **2020**, *262*, No. 114297.

(2) Wang, S.; Guo, H.; Li, Y.; Li, X. Penetration of Nanoparticles across a Lipid Bilayer: Effects of Particle Stiffness and Surface Hydrophobicity. *Nanoscale* **2019**, *11*, 4025−4034.

(3) Barbato, V.; Talevi, R.; Gualtieri, R.; Pallotta, M. M.; Di Nardo, M.; Costanzo, V.; Catapano, G.; Capriglione, T. Polystyrene Nanoparticles May Affect Cell Mitosis and Compromise Early Embryo Development in Mammals. *Theriogenology* **2020**, *145*, 18−23.

(4) Matthews, S.; Mai, L.; Jeong, C. B.; Lee, J. S.; Zeng, E. Y.; Xu, E. G. Key Mechanisms of Micro- and Nanoplastic (MNP) Toxicity across Taxonomic Groups. *Comp. Biochem. Physiol., Part C: Toxicol. Pharmacol.* **2021**, *247*, No. 109056.

(5) Briffa, S. M. Looking at the Bigger Picture—Considering the Hurdles in the Struggle against Nanoplastic Pollution. *Nanomaterials* **2021**, *11*, 2536.

(6) Tiede, K.; Hanssen, S. F.; Westerhoff, P.; Fern, G. J.; Hankin, S. M.; Aitken, R. J.; Chaudhry, Q.; Boxall, A. B. A. How Important Is Drinking Water Exposure for the Risks of Engineered Nanoparticles to Consumers? *Nanotoxicology* **2016**, *10*, 102−110.

(7) Park, C. M.; Chu, K. H.; Her, N.; Jang, M.; Baalousha, M.; Heo, J.; Yoon, Y. Occurrence and Removal of Engineered Nanoparticles in Drinking Water Treatment and Wastewater Treatment Processes. *Sep. Purif. Rev.* **2017**, *46*, 255−272.

(8) Bochicchio, D.; Cantu, L.; Cadario, M. V.; Palchetti, L.; Natali, F.; Monticelli, L.; Rossi, G.; Del Favero, E. Polystyrene Perturbs the Structure, Dynamics, and Mechanical Properties of DPPC Membranes: An Experimental and Computational Study. *J. Colloid Interface Sci.* **2022**, *605*, 110−119.

(9) Gigault, J.; Pedrono, B.; Maxit, B.; ter Halle, A. Marine Plastic Litter: The Unanalyzed Nano-Fraction. *Environ. Sci.: Nano* **2016**, *3*, 346−350.

(10) Lambert, S.; Wagner, M. Formation of Microscopic Particles during the Degradation of Different Polymers. *Chemosphere* **2016**, *161*, 510−517.

(11) Dawson, A. L.; Kawaguchi, S.; King, C. K.; Townsend, K. A.; King, R.; Huston, W. M.; Bengtson Nash, S. M. Turning Microplastics into Nanoplastics through Digestive Fragmentation by Antarctic Krill. *Nat. Commun.* **2018**, *9*, 1001.

(12) Martin, L. M. A.; Gan, N.; Wang, E.; Merrill, M.; Xu, W. Materials, Surfaces, and Interfacial Phenomena in Nanoplastics Toxicology Research. *Environ. Pollut.* **2022**, *292*, No. 118442.

(13) Brandts, I.; Teles, M.; Gonçalves, A. P.; Barreto, A.; Franco-Martinez, L.; Tvarijonaviciute, A.; Martins, M. A.; Soares, A. M. V. M.; Tort, L.; Oliveira, M. Effects of Nanoplastics on Mytilus Galloprovincialis after Individual and Combined Exposure with Carbamazepine. *Sci. Total Environ.* **2018**, *643*, 775−784.

(14) Canesi, L.; Ciacci, C.; Bergami, E.; Monopoli, M. P.; Dawson, K. A.; Papa, S.; Canonico, B.; Corsi, I. Evidence for Immunomodulation and Apoptotic Processes Induced by Cationic Polystyrene Nanoparticles in the Hemocytes of the Marine Bivalve Mytilus. *Mar. Environ. Res.* **2015**, *111*, 34−40.

(15) Varó, I.; Perini, A.; Torreblanca, A.; Garcia, Y.; Bergami, E.; Vannuccini, M. L.; Corsi, I. Time-Dependent Effects of Polystyrene Nanoparticles in Brine Shrimp Artemia Franciscana at Physiological, Biochemical and Molecular Levels. *Sci. Total Environ.* **2019**, *675*, 570−580.

(16) Bergami, E.; Krupinski Emerenciano, A.; González-Aravena, M.; Cárdenas, C. A.; Hernández, P.; Silva, J. R. M. C.; Corsi, I. Polystyrene Nanoparticles Affect the Innate Immune System of the Antarctic Sea Urchin Sterechinus Neumayeri. *Polar Biol.* **2019**, *42*, 743−757.

(17) Schultz, C. L.; Bart, S.; Lahive, E.; Spurgeon, D. J. What Is on the Outside Matters - Surface Charge and Dissolve Organic Matter Association Affect the Toxicity and Physiological Mode of Action of Polystyrene Nanoplastics to C. Elegans. *Environ. Sci. Technol.* **2021**, *55*, 6065−6075.

(18) Nazemidashtarjandi, S.; Vahedi, A.; Farnoud, A. M. Lipid Chemical Structure Modulates the Disruptive Effects of Nanomaterials on Membrane Models. *Langmuir* **2020**, *36*, 4923−4932.

(19) Contini, C.; Schneemilch, M.; Gaisford, S.; Quirke, N. Nanoparticle−Membrane Interactions. *J. Exp. Nanosci.* **2018**, *13*, 62−81.
(20) Contini, C.; Hindley, J. W.; Macdonald, T. J.; Barritt, J. D.; Ces, O.; Quirke, N. Size Dependency of Gold Nanoparticles Interacting with Model Membranes. *Commun. Chem.* **2020**, *3*, 130.
(21) Bennett, W. F. D.; Tieleman, D. P. The Importance of Membrane Defects—Lessons from Simulations. *Acc. Chem. Res.* **2014**, *47*, 2244−2251.
(22) Hollóczki, O.; Gehrke, S. Can Nanoplastics Alter Cell Membranes? *ChemPhysChem* **2020**, *21*, 9−12.
(23) Warren, E. A. K.; Payne, C. K. Cellular Binding of Nanoparticles Disrupts the Membrane Potential. *RSC Adv.* **2015**, *5*, 13660−13666.
(24) Xia, Z.; Woods, A.; Quirk, A.; Burgess, I. J.; Lau, B. L. T. Interactions between Polystyrene Nanoparticles and Supported Lipid Bilayers: Impact of Charge and Hydrophobicity Modification by Specific Anions. *Environ. Sci.: Nano* **2019**, *6*, 1829−1837.
(25) Lu, B.; Smith, T.; Schmidt, J. J. Nanoparticle-Lipid Bilayer Interactions Studied with Lipid Bilayer Arrays. *Nanoscale* **2015**, *7*, 7858−7866.
(26) Rascol, E.; Devoisselle, J. M.; Chopineau, J. The Relevance of Membrane Models to Understand Nanoparticles-Cell Membrane Interactions. *Nanoscale* **2016**, *8*, 4780−4798.
(27) Bailey, C. M.; Kamaloo, E.; Waterman, K. L.; Wang, K. F.; Nagarajan, R.; Camesano, T. A. Size Dependence of Gold Nanoparticle Interactions with a Supported Lipid Bilayer: A QCM-D Study. *Biophys. Chem.* **2015**, *203-204*, 51−61.
(28) Jing, B.; Zhu, Y. Disruption of Supported Lipid Bilayers by Semihydrophobic Nanoparticles. *J. Am. Chem. Soc.* **2011**, *133*, 10983−10989.
(29) Jing, B.; Abot, R. C. T.; Zhu, Y. Semihydrophobic Nanoparticle-Induced Disruption of Supported Lipid Bilayers: Specific Ion Effect. *J. Phys. Chem. B* **2014**, *118*, 13175−13182.
(30) Forte, M.; Iachetta, G.; Tussellino, M.; Carotenuto, R.; Prisco, M.; De Falco, M.; Laforgia, V.; Valiante, S. Polystyrene Nanoparticles Internalization in Human Gastric Adenocarcinoma Cells. *Toxicol. In Vitro* **2016**, *31*, 126−136.
(31) Negoda, A.; Kim, K. J.; Crandall, E. D.; Worden, R. M. Polystyrene Nanoparticle Exposure Induces Ion-Selective Pores in Lipid Bilayers. *Biochim. Biophys. Acta, Biomembr.* **2013**, *1828*, 2215−2222.
(32) Gurtovenko, A. A.; Anwar, J.; Vattulainen, I. Defect-Mediated Trafficking across Cell Membranes: Insights from in Silico Modeling. *Chem. Rev.* **2010**, *110*, 6077−6103.
(33) Meer, G. Membrane Lipids, Where They Are and How They Behave: Sphingolipids on the Move. *FASEB J.* **2010**, *24*, 312.1.
(34) Jacquemyn, J.; Cascalho, A.; Goodchild, R. E. The Ins and Outs of Endoplasmic Reticulum-controlled Lipid Biosynthesis. *EMBO Rep.* **2017**, *18*, 1905−1921.
(35) Van Meer, G.; Voelker, D. R.; Feigenson, G. W. Membrane Lipids: Where They Are and How They Behave. *Nat. Rev. Mol. Cell Biol.* **2008**, *9*, 112−124.
(36) Chen, E.; Kiebish, M. A.; McDaniel, J.; Gao, F.; Narain, N. R.; Sarangarajan, R.; Kacso, G.; Ravasz, D.; Seyfried, T. N.; Adam-Vizi, V.; Chinopoulos, C. The Total and Mitochondrial Lipidome of Artemia Franciscana Encysted Embryos. *Biochim. Biophys. Acta, Mol. Cell Biol. Lipids* **2016**, *1861*, 1727−1735.
(37) Navarro, J. C.; Amat, F.; Sargent, J. R. Lipid Composition of Cysts of the Brine Shrimp Artemia Sp. from Spanish Populations. *J. Exp. Mar. Biol. Ecol.* **1992**, *155*, 123−131.
(38) Navarro, J. C.; Bell, M. V.; Amat, F.; Sargent, J. R. The Fatty Acid Composition of Phospholipids from Brine Shrimp, Artemia Sp., Eyes. *Comp. Biochem. Physiol. Part B: Comp. Biochem.* **1992**, *103*, 89−91.
(39) Bergami, E.; Bocci, E.; Vannuccini, M. L.; Monopoli, M.; Salvati, A.; Dawson, K. A.; Corsi, I. Nano-Sized Polystyrene Affects Feeding, Behavior and Physiology of Brine Shrimp Artemia Franciscana Larvae. *Ecotoxicol. Environ. Saf.* **2016**, *123*, 18−25.
(40) Manfra, L.; Savorelli, F.; Di Lorenzo, B.; Libralato, G.; Comin, S.; Conti, D.; Floris, B.; Francese, M.; Gallo, M. L.; Gartner, I.; Guida, M.; Leoni, T.; Marino, G.; Martelli, F.; Palazzi, D.; Prato, E.; Righini, P.; Rossi, E.; Volpi Ghirardini, A.; Migliore, L. Intercalibration of Ecotoxicity Testing Protocols with Artemia Franciscana. *Ecol. Indic.* **2015**, *57*, 41−47.
(41) Libralato, G.; Prato, E.; Migliore, L.; Cicero, A. M.; Manfra, L. A Review of Toxicity Testing Protocols and Endpoints with Artemia Spp. *Ecol. Indic.* **2016**, *69*, 35−49.
(42) Perini, D. A.; Aguilella-Arzo, M.; Alcaraz, A.; Perálvarez-Marín, A.; Queralt-Martín, M. Dynorphin A Induces Membrane Permeabilization by Formation of Proteolipidic Pores. Insights from Electrophysiology and Computational Simulations. *Comput. Struct. Biotechnol. J.* **2022**, *20*, 230−240.
(43) Verdiá-Báguena, C.; Nieto-Torres, J. L.; Alcaraz, A.; Dediego, M. L.; Enjuanes, L.; Aguilella, V. M. Analysis of SARS-CoV e Protein Ion Channel Activity by Tuning the Protein and Lipid Charge. *Biochim. Biophys. Acta, Biomembr.* **2013**, *1828*, 2026−2031.
(44) Nieto-Torres, J. L.; DeDiego, M. L.; Verdiá-Báguena, C.; Jimenez-Guardeño, J. M.; Regla-Nava, J. A.; Fernandez-Delgado, R.; Castaño-Rodriguez, C.; Alcaraz, A.; Torres, J.; Aguilella, V. M.; Enjuanes, L. Severe Acute Respiratory Syndrome Coronavirus Envelope Protein Ion Channel Activity Promotes Virus Fitness and Pathogenesis. *PLoS Pathog.* **2014**, *10*, No. e1004077.
(45) Verdiá-Báguena, C.; Nieto-Torres, J. L.; Alcaraz, A.; DeDiego, M. L.; Torres, J.; Aguilella, V. M.; Enjuanes, L. Coronavirus E Protein Forms Ion Channels with Functionally and Structurally-Involved Membrane Lipids. *Virology* **2012**, *432*, 485−494.
(46) Verdiá-Báguena, C.; Aguilella, V. M.; Queralt-Martín, M.; Alcaraz, A. Transport Mechanisms of SARS-CoV-E Viroporin in Calcium Solutions: Lipid-Dependent Anomalous Mole Fraction Effect and Regulation of Pore Conductance. *Biochim. Biophys. Acta, Biomembr.* **2021**, *1863*, No. 183590.
(47) Gladue, D. P.; Holinka, L. G.; Largo, E.; Fernandez Sainz, I.; Carrillo, C.; O'Donnell, V.; Baker-Branstetter, R.; Lu, Z.; Ambroggio, X.; Risatti, G. R.; Nieva, J. L.; Borca, M. V. Classical Swine Fever Virus P7 Protein Is a Viroporin Involved in Virulence in Swine. *J. Virol.* **2012**, *86*, 6778−6791.
(48) Gladue, D. P.; Largo, E.; de la Arada, I.; Aguilella, V. M.; Alcaraz, A.; Arrondo, J. L. R.; Holinka, L. G.; Brocchi, E.; Ramirez-Medina, E.; Vuono, E. A.; Berggren, K. A.; Carrillo, C.; Nieva, J. L.; Borca, M. V. Molecular Characterization of the Viroporin Function of Foot-and-Mouth Disease Virus Nonstructural Protein 2B. *J. Virol.* **2018**, *92*, No. e01360-18.
(49) Largo, E.; Verdiá-Báguena, C.; Aguilella, V. M.; Nieva, J. L.; Alcaraz, A. Ion Channel Activity of the CSFV P7 Viroporin in Surrogates of the ER Lipid Bilayer. *Biochim. Biophys. Acta, Biomembr.* **2016**, *1858*, 30−37.
(50) Largo, E.; Gladue, D. P.; Torralba, J.; Aguilella, V. M.; Alcaraz, A.; Borca, M. V.; Nieva, J. L. Mutation-Induced Changes of Transmembrane Pore Size Revealed by Combined Ion-Channel Conductance and Single Vesicle Permeabilization Analyses. *Biochim. Biophys. Acta, Biomembr.* **2018**, *1860*, 1015−1021.
(51) Largo, E.; Queralt-Martín, M.; Carravilla, P.; Nieva, J. L.; Alcaraz, A. Single-Molecule Conformational Dynamics of Viroporin Ion Channels Regulated by Lipid-Protein Interactions. *Bioelectrochemistry* **2021**, *137*, No. 107641.
(52) Parra, E.; Alcaraz, A.; Cruz, A.; Aguilella, V. M.; Pérez-Gil, J. Hydrophobic Pulmonary Surfactant Proteins SP-B and SP-C Induce Pore Formation in Planar Lipid Membranes: Evidence for Proteolipid Pores. *Biophys. J.* **2013**, *104*, 146−155.
(53) Chen, K. L.; Bothun, G. D. Nanoparticles Meet Cell Membranes: Probing Nonspecific Interactions Using Model Membranes. *Environ. Sci. Technol.* **2014**, *48*, 873−880.
(54) Panalytical, M. Zeta Potential: An Introduction in 30 Minutes. *Zetasizer Nano Serles Tech. Note. TN101104* **2010**, *2*, 1−6.
(55) Parra-Ortiz, E.; Malekkhaiat Häffner, S.; Saerbeck, T.; Skoda, M. W. A.; Browning, K. L.; Malmsten, M. Oxidation of Polyunsaturated Lipid Membranes by Photocatalytic Titanium

Dioxide Nanoparticles: Role of PH and Salinity. *ACS Appl. Mater. Interfaces* **2020**, *12*, 32446−32460.
(56) Akbarzadeh, A.; Rezaei-Sadabady, R.; Davaran, S.; Joo, S. W.; Zarghami, N.; Hanifehpour, Y.; Samiei, M.; Kouhi, M.; Nejati-Koshki, K. Liposome: Classification, Preparation, and Applications. *Nanoscale Res. Lett.* **2013**, *8*, 102.
(57) Cho, N. J.; Frank, C. W.; Kasemo, B.; Hök, F. Quartz Crystal Microbalance with Dissipation Monitoring of Supported Lipid Bilayers on Various Substrates. *Nat. Protoc.* **2010**, *5*, 1096−1106.
(58) Malekkhaiat Häffner, S.; Parra-Ortiz, E.; Skoda, M. W. A.; Saerbeck, T.; Browning, K. L.; Malmsten, M. Composition Effects on Photooxidative Membrane Destabilization by TiO_2 Nanoparticles. *J. Colloid Interface Sci.* **2021**, *584*, 19−33.
(59) Häffner, S. M.; Parra-Ortiz, E.; Browning, K. L.; Jørgensen, E.; Skoda, M. W. A.; Montis, C.; Li, X.; Berti, D.; Zhao, D.; Malmsten, M. Membrane Interactions of Virus-like Mesoporous Silica Nanoparticles. *ACS Nano* **2021**, *15*, 6787−6800.
(60) Gerelli, Y.; Eriksson Skog, A.; Jephthah, S.; Welbourn, R. J. L.; Klechikov, A.; Skepö, M. Spontaneous Formation of Cushioned Model Membranes Promoted by an Intrinsically Disordered Protein. *Langmuir* **2020**, *36*, 3997−4004.
(61) Yousefi, N.; Wargenau, A.; Tufenkji, N. Toward More Free-Floating Model Cell Membranes: Method Development and Application to Their Interaction with Nanoparticles. *ACS Appl. Mater. Interfaces* **2016**, *8*, 14339−14348.
(62) Feiler, A. A.; Sahlholm, A.; Sandberg, T.; Caldwell, K. D. Adsorption and Viscoelastic Properties of Fractionated Mucin (BSM) and Bovine Serum Albumin (BSA) Studied with Quartz Crystal Microbalance (QCM-D). *J. Colloid Interface Sci.* **2007**, *315*, 475−481.
(63) Hök, F.; Kasemo, B.The QCM-D Technique for Probing Biomacromolecular Recognition Reactions. In *Piezoelectric Sensors*2006 (No. July 2006), pp 425 −447, DOI: 10.1007/5346_034.
(64) Reviakine, I.; Johannsmann, D.; Richter, R. P. Hearing What You Cannot See and Visualizing What You Hear: Interpreting Quartz Crystal Microbalance Data from Solvated Interfaces. *Anal. Chem.* **2011**, *83*, 8838−8848.
(65) Hök, F.; Kasemo, B.; Nylander, T.; Fant, C.; Sott, K.; Elwing, H. Variations in Coupled Water, Viscoelastic Properties, and Film Thickness of a Mefp-1 Protein Film during Adsorption and Cross-Linking: A Quartz Crystal Microbalance with Dissipation Monitoring, Ellipsometry, and Surface Plasmon Resonance Study. *Anal. Chem.* **2001**, *73*, 5796−5804.
(66) Bezrukov, S. M.; Vodyanoy, I. Probing Alamethicin Channels with Water-Soluble Polymers. Effect on Conductance of Channel States. *Biophys. J.* **1993**, *64*, 16−25.
(67) Montal, M.; Mueller, P. Formation of Bimolecular Membranes from Lipid Monolayers and a Study of Their Electrical Properties. *Proc. Natl. Acad. Sci. U. S. A.* **1972**, *69*, 3561−3566.
(68) Alcaraz, A.; Nestorovich, E. M.; López, M. L.; García-Giménez, E.; Bezrukov, S. M.; Aguilella, V. M. Diffusion, Exclusion, and Specific Binding in a Large Channel: A Study of OmpF Selectivity Inversion. *Biophys. J.* **2009**, *96*, 56−66.
(69) Hodgkin, A. L.; Katz, B. The Effect of Sodium Ions on the Electrical Activity of the Giant Axon of the Squid. *J. Physiol.* **1949**, *108*, 37−77.
(70) Magsphere INC. *Plain polystyrene*.
(71) Zhang, X.; Yang, S. Nonspecific Adsorption of Charged Quantum Dots on Supported Zwitterionic Lipid Bilayers: Real-Time Monitoring by Quartz Crystal Microbalance with Dissipation. *Langmuir* **2011**, *27*, 2528−2535.
(72) Santos-Martinez; Inkielewicz-Stepniak, I.; Medina, C.; Rahme, K.; D'Arcy, D.; Fox, D.; Holmes, J.; Zhang, H.; Radomski, M. W. The Use of Quartz Crystal Microbalance with Dissipation (QCM-D) for Studying Nanoparticle-Induced Platelet Aggregation. *Int. J. Nanomed.* **2012**, *7*, 243.
(73) Hök, F.; Rodahl, M.; Brzezinski, P.; Kasemo, B.*Energy Dissipation Kinetics for Protein and Antibody-Antigen Adsorption under Shear Oscillation on a Quartz Crystal Microbalance*; 1998.
(74) Grammou, A.; Samaras, P.; Papadimitriou, C.; Papadopoulos, A. I. Ecotoxicology and Environmental Safety A Test for Adequate Wastewater Treatment Based on Glutathione S Transferase Isoenzyme Profile. *Ecotoxicol. Environ. Saf.* **2013**, *90*, 46−51.
(75) Madhav, M. R.; David, S. E. M.; Kumar, R. S. S.; Swathy, J. S.; Bhuvaneshwari, M.; Mukherjee, A.; Chandrasekaran, N. Toxicity and Accumulation of Copper Oxide (CuO) Nanoparticles in Different Life Stages of Artemia Salina. *Environ. Toxicol. Pharmacol.* **2017**, *52*, 227−238.
(76) Arulvasu, C.; Jennifer, S. M.; Prabhu, D.; Chandhirasekar, D. Toxicity Effect of Silver Nanoparticles in Brine Shrimp Artemia. *Sci. World J.* **2014**, *2014*, No. 256919.
(77) Nielsen, S. B.; Otzen, D. E. Quartz Crystal Microbalances as Tools for Probing Protein−Membrane Interactions. *Methods Mol. Biol.* **2019**, *2003*, 31−52.
(78) Richter, R.; Mukhopadhyay, A.; Brisson, A. Pathways of Lipid Vesicle Deposition on Solid Surfaces: A Combined QCM-D and AFM Study. *Biophys. J.* **2003**, *85*, 3035−3047.
(79) Lind, T. K.; Wacklin, H.; Schiller, J.; Moulin, M.; Haertlein, M.; Pomorski, T. G.; Cárdenas, M. Formation and Characterization of Supported Lipid Bilayers Composed of Hydrogenated and Deuterated Escherichia Coli Lipids. *PLoS One* **2015**, *10*, No. e0144671.
(80) Armanious, A.; Agnarsson, B.; Lundgren, A.; Zhdanov, V. P.; Hök, F. Determination of Nanosized Adsorbate Mass in Solution Using Mechanical Resonators: Elimination of the so Far Inseparable Liquid Contribution. *J. Phys. Chem. C* **2021**, *125*, 22733−22746.
(81) Paul, S.; Paul, D.; Basova, T.; Ray, A. K. Studies of Adsorption and Viscoelastic Properties of Proteins onto Liquid Crystal Phthalocyanine Surface Using Quartz Crystal Microbalance with Dissipation Technique. *J. Phys. Chem. C* **2008**, *112*, 11822−11830.
(82) Wan, F.; Nylander, T.; Foged, C.; Yang, M.; Baldursdottir, S. G.; Nielsen, H. M. Qualitative and Quantitative Analysis of the Biophysical Interaction of Inhaled Nanoparticles with Pulmonary Surfactant by Using Quartz Crystal Microbalance with Dissipation Monitoring. *J. Colloid Interface Sci.* **2019**, *545*, 162−171.
(83) Peh, W. Y. X.; Reimhult, E.; Teh, H. F.; Thomsen, J. S.; Su, X. Understanding Ligand Binding Effects on the Conformation of Estrogen Receptor α-DNA Complexes: A Combinational Quartz Crystal Microbalance with Dissipation and Surface Plasmon Resonance Study. *Biophys. J.* **2007**, *92*, 4415−4423.
(84) Tagaya, M. In Situ QCM-D Study of Nano-Bio Interfaces with Enhanced Biocompatibility. *Polym. J.* **2015**, *47*, 599−608.
(85) Kunze, A.; Svedhem, S.; Kasemo, B. Lipid Transfer between Charged Supported Lipid Bilayers and Oppositely Charged Vesicles. *Langmuir* **2009**, *25*, 5146−5158.
(86) Malekkhaiat Häffner, S.; Nyström, L.; Nordström, R.; Xu, Z. P.; Davoudi, M.; Schmidtchen, A.; Malmsten, M. Membrane Interactions and Antimicrobial Effects of Layered Double Hydroxide Nanoparticles. *Phys. Chem. Chem. Phys.* **2017**, *19*, 23832−23842.
(87) Leroueil, P. R.; Berry, S. A.; Duthie, K.; Han, G.; Rotello, V. M.; McNerny, D. Q.; Baker, J. R.; Orr, B. G.; Holl, M. M. B. Wide Varieties of Cationic Nanoparticles Induce Defects in Supported Lipid Bilayers. *Nano Lett.* **2008**, *8*, 420−424.
(88) Priest, L.; Peters, J. S.; Kukura, P. Scattering-Based Light Microscopy: From Metal Nanoparticles to Single Proteins. *Chem. Rev.* **2021**, *121*, 11937−11970.
(89) Liu, P.; Zabala-Ferrera, O.; Beltramo, P. J. Fabrication and Electromechanical Characterization of Freestanding Asymmetric Membranes. *Biophys. J.* **2021**, *120*, 1755−1764.
(90) López, M. L.; Queralt-Martín, M.; Alcaraz, A. Stochastic Pumping of Ions Based on Colored Noise in Bacterial Channels under Acidic Stress. *Nanoscale* **2016**, *8*, 13422−13428.
(91) Stein, R. B.; Stein, R. B.Membrane Permeability and Voltage. In *Nerve and Muscle*; Springer US: Boston, MA, 1980; pp. 33−44, DOI: 10.1007/978-1-4684-3797-3_4.
(92) Cahalan, M. D.; Chandy, K. G. The Functional Network of Ion Channels in T Lymphocytes. *Immunol. Rev.* **2009**, *231*, 59−87.

(93) Li, S.; Malmstadt, N. Deformation and Poration of Lipid Bilayer Membranes by Cationic Nanoparticles. *Soft Matter* **2013**, *9*, 4969−4976.
(94) van der Wel, C.; Heinrich, D.; Kraft, D. J. Microparticle Assembly Pathways on Lipid Membranes. *Biophys. J.* **2017**, *113*, 1037−1046.
(95) Yu, Y.; Granick, S. Pearling of Lipid Vesicles Induced by Nanoparticles. *J. Am. Chem. Soc.* **2009**, *131*, 14158−14159.
(96) Hille, B.*Ion Channels of Excitable Membranes*, 3rd ed.; Sinauer Associates Inc: Sunderland, MA, 2001; Vol. Third Edit.
(97) Ramachandran, S.; Merrill, N. E.; Blick, R. H.; van der Weide, D. W. Colloidal Quantum Dots Initiating Current Bursts in Lipid Bilayers. *Biosens. Bioelectron.* **2005**, *20*, 2173−2176.
(98) Tristram-Nagle, S.; Kim, D. J.; Akhunzada, N.; Kuerka, N.; Mathai, J. C.; Katsaras, J.; Zeidel, M.; Nagle, J. F. Structure and Water Permeability of Fully Hydrated DiphytanoylPC. *Chem. Phys. Lipids* **2010**, *163*, 630−637.
(99) Derakhshankhah, H.; Jafari, S. Cell Penetrating Peptides: A Concise Review with Emphasis on Biomedical Applications. *Biomed. Pharmacother.* **2018**, *108*, 1090−1096.
(100) Gilbert, R. J. C.; Serra, M. D.; Froelich, C. J.; Wallace, M. I.; Anderluh, G. Membrane Pore Formation at Protein−Lipid Interface. *Trends Biochem. Sci.* **2014**, *39*, 510−516.
(101) Kullman, L.; Gurnev, P. A.; Winterhalter, M.; Bezrukov, S. M. Functional Subconformations in Protein Folding: Evidence from Single-Channel Experiments. *Phys. Rev. Lett.* **2006**, *96*, No. 038101.
(102) Mielke, M.; Zimchl, R. Measures to Determine the Hydrophobicity of Colloidal Polymers. *Prog. Colloid Polym. Sci.* **2002**, *117*, 56−62.
(103) Muller, R. H.; Davis, S. S.; Illum, L.; Mak, E.Particle Charge and Surface Hydrophobicity of Colloidal Drug Carriers. In *Target. Drugs With Synth. Syst.*, 1986; pp 239−263, DOI: 10.1007/978-1-4684-5185-6_18.
(104) Chen, C.-S.; Chung, W.-J.; Hsu, I. C.; Wu, C.-M.; Chin, W.-C. Force Field Measurements within the Exclusion Zone of Water. *J. Biol. Phys.* **2012**, *38*, 113−120.
(105) Fadda, G. C.; Lairez, D.; Zalczer, G. Fluctuations of Ionic Current Through Lipid Bilayers at the Onset of Peptide Attacks and Pore Formation. *Phys. Rev. Lett.* **2009**, *103*, No. 180601.
(106) Gazit, E.; Boman, A.; Boman, H. G.; Shai, Y. Interaction of the Mammalian Antibacterial Peptide Cecropin P1 with Phospholipid Vesicles. *Biochemistry* **1995**, *34*, 11479−11488.
(107) Alcaraz, A.; Ramírez, P.; García-Giménez, E.; López, M. L.; Andrio, A.; Aguilella, V. M. A PH-Tunable Nanofluidic Diode: Electrochemical Rectification in a Reconstituted Single Ion Channel. *J. Phys. Chem. B* **2006**, *110*, 21205−21209.
(108) García-Giménez, E.; Alcaraz, A.; Aguilella, V. M.; Ramírez, P. Directional Ion Selectivity in a Biological Nanopore with Bipolar Structure. *J. Membr. Sci.* **2009**, *331*, 137−142.
(109) López-León, T.; Jódar-Reyes, A. B.; Bastos-González, D.; Ortega-Vinuesa, J. L. Hofmeister Effects in the Stability and Electrophoretic Mobility of Polystyrene Latex Particles. *J. Phys. Chem. B* **2003**, *107*, 5696−5708.
(110) Xia, Z.; Lau, B. L. T. Mitigating Effects of Osmolytes on the Interactions between Nanoparticles and Supported Lipid Bilayer. *J. Colloid Interface Sci.* **2020**, *568*, 1−7.
(111) Lee, H.; Malmstadt, N. Effect of Low Levels of Lipid Oxidation on the Curvature, Dynamics, and Permeability of Lipid Bilayers and Their Interactions with Cationic Nanoparticles. *J. Phys. D: Appl. Phys.* **2018**, *51*, 164002.
(112) Nag, O. K.; Muroski, M. E.; Hastman, D. A.; Almeida, B.; Medintz, I. L.; Huston, A. L.; Delehanty, J. B. Nanoparticle-Mediated Visualization and Control of Cellular Membrane Potential: Strategies, Progress, and Remaining Issues. *ACS Nano* **2020**, *14*, 2659−2677.
(113) Khater, M. S.; Kulkarni, G. R.; Khater, S. S.; Gholap, H.; Patil, R. Study to Elucidate Effect of Titanium Dioxide Nanoparticles on Bacterial Membrane Potential and Membrane Permeability. *Mater. Res. Express* **2020**, *7*, No. 035005.
(114) Roshanzadeh, A.; Oyunbaatar, N. E.; Ganjbakhsh, S. E.; Park, S.; Kim, D. S.; Kanade, P. P.; Lee, S.; Lee, D. W.; Kim, E. S. Exposure to Nanoplastics Impairs Collective Contractility of Neonatal Cardiomyocytes under Electrical Synchronization. *Biomaterials* **2021**, *278*, No. 121175.
(115) Ziglari, T.; Wang, Z.; Holian, A. Contribution of Particle-Induced Lysosomal Membrane Hyperpolarization to Lysosomal Membrane Permeabilization. *Int. J. Mol. Sci.* **2021**, *22*, 2277.
(116) Farnoud, A. M.; Nazemidashtarjandi, S. Emerging Investigator Series: Interactions of Engineered Nanomaterials with the Cell Plasma Membrane; What Have We Learned from Membrane Models? *Environ. Sci.: Nano* **2019**, *6*, 13−40.
(117) Ruenraroengsak, P.; Tetley, T. D. Differential Bioreactivity of Neutral, Cationic and Anionic Polystyrene Nanoparticles with Cells from the Human Alveolar Compartment: Robust Response of Alveolar Type 1 Epithelial Cells. *Part. Fibre Toxicol.* **2015**, *12*, 19.
(118) Yu, S. P.; Canzoniero, L. M. T.; Choi, D. W. Ion Homeostasis and Apoptosis. *Curr. Opin. Cell Biol.* **2001**, *13*, 405−411.
(119) Yang, J.; Yu, G.; Sessler, J. L.; Shin, I.; Gale, P. A.; Huang, F. Artificial Transmembrane Ion Transporters as Potential Therapeutics. *Chem* **2021**, *7*, 3256−3291.

https://doi.org/10.1021/acs.langmuir.2c02487
Langmuir 2022, 38, 14837−14849